

# Measurement of the radiative neutron capture cross section of $^{206}\text{Pb}$ and its astrophysical implications

C. Domingo-Pardo,<sup>1,2,\*</sup> U. Abbondanno,<sup>3</sup> G. Aerts,<sup>4</sup> H. Álvarez,<sup>5</sup> F. Alvarez-Velarde,<sup>6</sup> S. Andriamonje,<sup>4</sup> J. Andrzejewski,<sup>7</sup> P. Assimakopoulos,<sup>8</sup> L. Audouin,<sup>1</sup> G. Badurek,<sup>9</sup> P. Baumann,<sup>10</sup> F. Bečvář,<sup>11</sup> E. Berthoumieux,<sup>4</sup> S. Bisterzo,<sup>12,1</sup> F. Calviño,<sup>13</sup> M. Calviani,<sup>14</sup> D. Cano-Ott,<sup>6</sup> R. Capote,<sup>15,16</sup> C. Carrapiço,<sup>17</sup> P. Cennini,<sup>18</sup> V. Chepel,<sup>19</sup> E. Chiaveri,<sup>18</sup> N. Colonna,<sup>20</sup> G. Cortes,<sup>13</sup> A. Couture,<sup>21</sup> J. Cox,<sup>21</sup> M. Dahlfors,<sup>18</sup> S. David,<sup>10</sup> I. Dillman,<sup>1</sup> R. Dolfini,<sup>22</sup> W. Dridi,<sup>4</sup> I. Duran,<sup>5</sup> C. Eleftheriadis,<sup>23</sup> M. Embid-Segura,<sup>6</sup> L. Ferrant,<sup>24</sup> A. Ferrari,<sup>18</sup> R. Ferreira-Marques,<sup>19</sup> L. Fitzpatrick,<sup>18</sup> H. Fraiss-Koelbl,<sup>25</sup> K. Fujii,<sup>3</sup> W. Furman,<sup>26</sup> R. Gallino,<sup>12</sup> I. Goncalves,<sup>17</sup> E. Gonzalez-Romero,<sup>6</sup> A. Goverdovski,<sup>27</sup> F. Gramegna,<sup>14</sup> E. Griesmayer,<sup>25</sup> C. Guerrero,<sup>6</sup> F. Gunsing,<sup>4</sup> B. Haas,<sup>28</sup> R. Haight,<sup>29</sup> M. Heil,<sup>1</sup> A. Herrera-Martinez,<sup>18</sup> M. Igashira,<sup>30</sup> M. Isaev,<sup>24</sup> E. Jericha,<sup>9</sup> F. Käppeler,<sup>1</sup> Y. Kadi,<sup>18</sup> D. Karadimos,<sup>8</sup> D. Karamanis,<sup>8</sup> M. Kerveno,<sup>10</sup> V. Ketlerov,<sup>27,18</sup> P. Koehler,<sup>31</sup> V. Konovalov,<sup>26,18</sup> E. Kossionides,<sup>32</sup> M. Krčička,<sup>11</sup> C. Lamboudis,<sup>23</sup> H. Leeb,<sup>9</sup> A. Lindote,<sup>19</sup> I. Lopes,<sup>19</sup> M. Lozano,<sup>16</sup> S. Lukic,<sup>10</sup> J. Marganec,<sup>7</sup> S. Marrone,<sup>20</sup> C. Massimi,<sup>33</sup> P. Mastinu,<sup>14</sup> A. Mengoni,<sup>34,18</sup> P.M. Milazzo,<sup>3</sup> C. Moreau,<sup>3</sup> M. Mosconi,<sup>1</sup> F. Neves,<sup>19</sup> H. Oberhummer,<sup>9</sup> M. Oshima,<sup>35</sup> S. O'Brien,<sup>21</sup> J. Pancin,<sup>4</sup> C. Papachristodoulou,<sup>8</sup> C. Papadopoulos,<sup>36</sup> C. Paradela,<sup>5</sup> N. Patronis,<sup>8</sup> A. Pavlik,<sup>37</sup> P. Pavlopoulos,<sup>38</sup> L. Perrot,<sup>4</sup> R. Plag,<sup>1</sup> A. Plompen,<sup>39</sup> A. Plukis,<sup>4</sup> A. Poch,<sup>13</sup> C. Pretel,<sup>13</sup> J. Quesada,<sup>16</sup> T. Rauscher,<sup>40</sup> R. Reifarh,<sup>29</sup> M. Rosetti,<sup>41</sup> C. Rubbia,<sup>22</sup> G. Rudolf,<sup>10</sup> P. Rullhusen,<sup>39</sup> J. Salgado,<sup>17</sup> L. Sarchiapone,<sup>18</sup> I. Savvidis,<sup>23</sup> C. Stephan,<sup>24</sup> G. Tagliente,<sup>20</sup> J.L. Tain,<sup>2</sup> L. Tassan-Got,<sup>24</sup> L. Tavora,<sup>17</sup> R. Terlizzi,<sup>20</sup> G. Vannini,<sup>33</sup> P. Vaz,<sup>17</sup> A. Ventura,<sup>41</sup> D. Villamarin,<sup>6</sup> M.C. Vincente,<sup>6</sup> V. Vlachoudis,<sup>18</sup> R. Vlastou,<sup>36</sup> F. Voss,<sup>1</sup> S. Walter,<sup>1</sup> H. Wendler,<sup>18</sup> M. Wiescher,<sup>21</sup> and K. Wisshak<sup>1</sup>

(The n-TOF Collaboration)

<sup>1</sup>Forschungszentrum Karlsruhe GmbH (FZK), Institut für Kernphysik, Germany

<sup>2</sup>Instituto de Física Corpuscular, CSIC-Universidad de Valencia, Spain

<sup>3</sup>Istituto Nazionale di Fisica Nucleare (INFN), Trieste, Italy

<sup>4</sup>CEA/Saclay - DSM/DAPNIA, Gif-sur-Yvette, France

<sup>5</sup>Universidade de Santiago de Compostela, Spain

<sup>6</sup>Centro de Investigaciones Energeticas Medioambientales y Tecnologicas, Madrid, Spain

<sup>7</sup>University of Lodz, Lodz, Poland

<sup>8</sup>University of Ioannina, Greece

<sup>9</sup>Atominstytut der Österreichischen Universitäten, Technische Universität Wien, Austria

<sup>10</sup>Centre National de la Recherche Scientifique/IN2P3 - IReS, Strasbourg, France

<sup>11</sup>Charles University, Prague, Czech Republic

<sup>12</sup>Dipartimento di Fisica Generale, Università di Torino, Italy

<sup>13</sup>Universitat Politècnica de Catalunya, Barcelona, Spain

<sup>14</sup>Istituto Nazionale di Fisica Nucleare (INFN), Laboratori Nazionali di Legnaro, Italy

<sup>15</sup>International Atomic Energy Agency, NAPC/Nuclear Data Section, Vienna, Austria

<sup>16</sup>Universidad de Sevilla, Spain

<sup>17</sup>Instituto Tecnológico e Nuclear (ITN), Lisbon, Portugal

<sup>18</sup>CERN, Geneva, Switzerland

<sup>19</sup>LIP - Coimbra & Departamento de Física da Universidade de Coimbra, Portugal

<sup>20</sup>Istituto Nazionale di Fisica Nucleare (INFN), Bari, Italy

<sup>21</sup>University of Notre Dame, Notre Dame, USA

<sup>22</sup>Università degli Studi di Pavia, Pavia, Italy

<sup>23</sup>Aristotle University of Thessaloniki, Greece

<sup>24</sup>Centre National de la Recherche Scientifique/IN2P3 - IPN, Orsay, France

<sup>25</sup>Fachhochschule Wiener Neustadt, Wiener Neustadt, Austria

<sup>26</sup>Joint Institute for Nuclear Research, Frank Laboratory of Neutron Physics, Dubna, Russia

<sup>27</sup>Institute of Physics and Power Engineering, Kaluga region, Obninsk, Russia

<sup>28</sup>Centre National de la Recherche Scientifique/IN2P3 - CENBG, Bordeaux, France

<sup>29</sup>Los Alamos National Laboratory, New Mexico, USA

<sup>30</sup>Tokyo Institute of Technology, Tokyo, Japan

<sup>31</sup>Oak Ridge National Laboratory, Physics Division, Oak Ridge, USA

<sup>32</sup>NCSR, Athens, Greece

<sup>33</sup>Dipartimento di Fisica, Università di Bologna, and Sezione INFN di Bologna, Italy

<sup>34</sup>International Atomic Energy Agency (IAEA), NAPC/Nuclear Data Section, Vienna, Austria

<sup>35</sup>Japan Atomic Energy Research Institute, Tokai-mura, Japan

<sup>36</sup>National Technical University of Athens, Greece

<sup>37</sup>Institut für Isotopenforschung und Kernphysik, Universität Wien, Austria

<sup>38</sup>Pôle Universitaire Léonard de Vinci, Paris La Défense, France

<sup>39</sup>CEC-JRC-IRMM, Geel, Belgium

<sup>40</sup>Department of Physics and Astronomy - University of Basel, Basel, Switzerland

<sup>41</sup>ENEA, Bologna, Italy

(Dated: November 1, 2018)

The  $(n, \gamma)$  cross section of  $^{206}\text{Pb}$  has been measured at the CERN n\_TOF facility with high resolution in the energy range from 1 eV to 620 keV by using two optimized  $\text{C}_6\text{D}_6$  detectors. In the investigated energy interval about 130 resonances could be observed, from which 61 had enough statistics to be reliably analyzed via the R-matrix analysis code SAMMY. Experimental uncertainties were minimized, in particular with respect to (i) angular distribution effects of the prompt capture  $\gamma$ -rays, and to (ii) the TOF-dependent background due to sample-scattered neutrons. Other background components were addressed by background measurements with an enriched  $^{208}\text{Pb}$  sample. The effect of the lower energy cutoff in the pulse height spectra of the  $\text{C}_6\text{D}_6$  detectors was carefully corrected via Monte Carlo simulations. Compared to previous  $^{206}\text{Pb}$  values, the Maxwellian averaged capture cross sections derived from these data are about 20% and 9% lower at thermal energies of 5 keV and 30 keV, respectively. These new results have a direct impact on the  $s$ -process abundance of  $^{206}\text{Pb}$ , which represents an important test for the interpretation of the cosmic clock based on the decay of  $^{238}\text{U}$ .

PACS numbers: 25.40.Lw, 27.80.+w, 97.10.Cv

Keywords: Neutron capture cross sections; Nuclear astrophysics; Pulse height weighting technique;  $\text{C}_6\text{D}_6$  scintillation detectors; Monte Carlo simulations

## I. INTRODUCTION

Similar to the majority of the stable isotopes beyond iron,  $^{206,207,208}\text{Pb}$  and  $^{209}\text{Bi}$  are synthesized by the rapid ( $r$ -) and slow ( $s$ -) neutron capture processes. However, this mass region is particularly interesting because the  $r$ -process abundances are dominated by the decay of the short lived  $\alpha$ -unstable transbismuth isotopes [1]. This feature provides an important consistency check for the  $r$ -process abundance calculations in the actinide region, since the integrated  $r$  residuals are constrained by the difference between the solar abundance values and the respective  $s$ -process components. Reliable  $r$ -process calculations are required for the interpretation of the observed Th and U abundances in the ultra metal-poor (UMP) stars of the Galactic halo. Since these stars are considered to be as old as the Galaxy, the observed Th and U abundances can be used as cosmo-chronometers, provided the original Th and U abundances are inferred from  $r$ -process models. This dating mechanism has the advantage of being independent of the yet uncertain  $r$ -process site [1, 2, 3].

Apart from its relevance for establishing the basic constraints for the  $r$ -process chronometry in general,  $^{206}\text{Pb}$  contains also dating information in itself. The  $^{206}\text{Pb}/^{238}\text{U}$  cosmo-chronometer was first introduced by Clayton in 1964 [4]. The  $^{238}\text{U}$  produced by the  $r$  process decays with a half life of  $t_{1/2} = 4.5 \times 10^9$  yr over a chain of  $\alpha$  and  $\beta$  decays ending at  $^{206}\text{Pb}$ . Therefore, its radiogenic abundance component,  $N_c^{206}$ , can be used to constrain the age of the parent isotope  $^{238}\text{U}$ , and hence the age ( $\Delta_r$ ) of the  $r$ -process. Unlike the more direct  $r$ -process abundance predictions derived from the Th and

U abundances in UMP stars, this procedure requires a Galactic evolution model, which describes the supernova rate or the frequency of the  $r$ -process events [5]. The drawback of this clock arises from the difficulty to isolate the cosmo-radiogenic component of  $^{206}\text{Pb}$  accurately enough from the additional abundance components.

Apart from these astrophysical aspects, the neutron capture cross section of  $^{206}\text{Pb}$  is also of importance for the design of fast reactor systems based on a Pb/Bi spallation source. Because 24.1% of natural lead consists of  $^{206}\text{Pb}$ , its  $(n, \gamma)$  cross section influences the neutron balance of the reactor [6].

There have been several measurements of the  $^{206}\text{Pb}(n, \gamma)$  cross section, which show discrepancies that are difficult to understand (see Sec. IV A). The aim of this work is to perform a new independent measurement with higher accuracy and in this way to determine the  $s$ -process contribution to the  $^{206}\text{Pb}$  abundance,  $N_s^{206}$ , more reliably.

In fact, the  $s$ -process abundance of this isotope is almost completely determined by the stellar  $(n, \gamma)$  cross section, nearly independent of the stellar model used [7]. Therefore, the uncertainty of  $N_s^{206}$  arises mostly from the cross section uncertainty.

Potential sources of systematic error have been substantially reduced in the present measurement, which was performed at the CERN n\_TOF installation. The new setup, and in particular the detectors themselves, were optimized for very low neutron sensitivity. Furthermore, the detectors were mounted at  $\sim 125^\circ$  with respect to the incident neutron beam in order to minimize the correction for angular distribution effects. The experimental details are presented in Sec. II, followed by the adopted data analysis procedures and an evaluation of the various systematic uncertainties in Sec. III. The deduced resonance parameters and the corresponding Maxwellian averaged capture cross sections in the stellar temperature

---

\*Corresponding author. E-mail: cesar.domingo.pardo@cern.ch

regime are presented in Sec. IV. Based on these new data, first astrophysical implications for the  $s$ -process abundance of  $^{206}\text{Pb}$  are discussed in Sec. V.

## II. MEASUREMENT

The time-of-flight (TOF) measurement was performed at the CERN n\_TOF installation [8] using a set of two  $\text{C}_6\text{D}_6$  detectors. Neutrons were produced by a 20 GeV proton beam on a lead spallation target. The spallation source was surrounded by a 6 cm thick water layer, which served as a coolant and as a moderator for the initially fast neutron spectrum. The beam was characterized by intense bunches of  $(3 \text{ to } 7) \times 10^{12}$  protons, a width of 6 ns (rms), and a repetition rate of only 0.4 Hz. This extremely low duty-cycle allows one to perform  $(n, \gamma)$  measurements over a broad neutron energy interval from 1 eV up to 1 MeV and to achieve favorable background conditions. Data were recorded by means of an advanced acquisition system with zero dead time, based on 8 bit Flash-Analog-to-Digital Converters (FADC), with 500 MHz sampling rate and 8 MB buffer memory [9].

The measurement was performed with an enriched metal sample 8.123 g in mass and 20 mm in diameter. The sample was enriched to 99.76% in  $^{206}\text{Pb}$  with small impurities of  $^{207}\text{Pb}$  (0.21%) and  $^{208}\text{Pb}$  (0.03%).

Capture events were registered with two  $\text{C}_6\text{D}_6$   $\gamma$ -ray detectors optimized for very low neutron sensitivity [10]. A sketch of the experimental setup is shown in Fig. 2 of Ref. [11]. The absolute value of the neutron fluence was determined by regular calibration measurements with an 0.5 mm thick gold sample and by using the saturated resonance technique [12] for the first gold resonance at  $E_n = 4.9$  eV. The energy differential neutron flux was determined with a relative uncertainty of  $\pm 2\%$  from the flux measurement with a  $^{235,238}\text{U}$  fission chamber calibrated by Physikalisch-Technische Bundesanstalt (PTB) [13]. The neutron intensity at the sample position was also monitored by means of a  $200\text{-}\mu\text{g}/\text{cm}^2$  thick  $^6\text{Li}$  foil in the neutron beam about 2.5 m upstream of the capture sample. The  $^6\text{Li}$  foil was surrounded by four silicon detectors outside of the beam for recording the  $^3\text{H}$  and  $\alpha$  particles from the  $(n, \alpha)$  reactions.

Compared to previous measurements [14, 15], the present setup had the advantage that the detectors were placed at  $\sim 125^\circ$  with respect to the incident neutron beam. In this way, the corrections for angular distribution effects of the prompt capture  $\gamma$ -rays were strongly reduced. This configuration led also to a substantial reduction of the background from in-beam  $\gamma$ -rays scattered in the sample [16].

## III. CAPTURE DATA ANALYSIS

The response function of the  $\text{C}_6\text{D}_6$  detectors needs to be modified such that the detection probability for capture cascades becomes independent of the cascade multipolarity. This was accomplished by application of the Pulse Height Weighting Technique (PHWT) [17]. Based on previous experience [11, 18, 19], the weighting functions (WFs) for the gold and lead samples were obtained by means of Monte Carlo calculations. The accuracy of the WFs was verified with the method described in Ref. [18], by which the calculated WFs were applied to Monte Carlo simulated capture  $\gamma$ -ray spectra. Using this procedure, the uncertainty of the WFs was estimated to be smaller than 0.5% for the samples used in the present experiment.

The weighted count rate  $N^w$  is then transformed into an experimental yield,

$$Y^{exp} = f^{sat} \frac{N^w}{N_n E_c}, \quad (1)$$

where the yield-normalization factor  $f^{sat}$  is determined by calibration measurements using the saturated 4.9 eV resonance in gold.  $N_n$  denotes the neutron flux and  $E_c$  the effective binding energy.

The yield in Eq. (1) is still subject to several corrections. The common effects of the background and of the low energy cutoff in the pulse height spectra of the  $\gamma$  detectors are described in Secs. III A and III B, respectively. The measurement on  $^{206}\text{Pb}$  is particularly sensitive to the angular distribution of the prompt capture  $\gamma$ -rays. The impact of this effect is described in Sec. III C.

### A. Backgrounds

A major source of background is due to in-beam  $\gamma$ -rays, predominantly from neutron captures in the water moderator, which travel along the neutron flight tube and are scattered in the  $^{206}\text{Pb}$  sample. This background exhibits a smooth dependence on neutron energy, with a broad maximum around  $E_n \approx 10$  keV. The shape of this background was determined from the spectrum measured with an isotopically pure  $^{208}\text{Pb}$  sample, which contains practically no resonances in the investigated neutron energy range. This spectrum was properly scaled and used as a point-wise numerical function in the R-matrix analysis of the  $^{206}\text{Pb}$  capture yield (see Sec. IV).

Another type of background arises in the analysis of resonances with a dominant neutron scattering channel,  $\Gamma_n \gg \Gamma_\gamma$ . In such cases, there are about  $\Gamma_n/\Gamma_\gamma$  scattered neutrons per capture event. These scattered neutrons can be captured in the detectors or in surrounding materials, thus mimicking true capture events. This effect was estimated to be negligible for all the resonances listed in Table II.

## B. Digital threshold

As mentioned in Sec. II, FADCs were used for recording directly the analog output signals of the C<sub>6</sub>D<sub>6</sub> detectors. Without any further discrimination, 8 MB of data would have been acquired per proton pulse in each detector. Depending on the sample, this enormous amount of data could be reduced by factors of 20 to 100 by using a zero suppression algorithm (see Ref. [9] for details). By this method events below a certain pulse-height are discriminated by a constant digital threshold analogous to conventional data acquisition systems, where an electronic threshold is used to reduce backgrounds and dead time effects.

Due to this threshold, the pulse height spectra of the C<sub>6</sub>D<sub>6</sub> detectors exhibit a low energy cutoff at a certain value of the signal amplitude (see Fig. 1). In this experiment the threshold was set at a  $\gamma$ -ray energy of 320 keV. If the pulse height spectra of the <sup>206</sup>Pb sample and of the gold sample used for normalization would have the same shape, the fraction of weighted counts below this threshold would nearly cancel out in the expression for the yield,

$$Y^{exp} \propto \frac{\sum_{0keV}^{320 keV} W_i^{Pb} R_i^{Pb} + \sum_{320 keV}^{E_c} W_i^{Pb} R_i^{Pb}}{\sum_{0keV}^{320 keV} W_i^{Au} R_i^{Au} + \sum_{320 keV}^{E_c} W_i^{Au} R_i^{Au}} \approx \frac{\sum_{320 keV}^{E_c} W_i^{Pb} R_i^{Pb}}{\sum_{320 keV}^{E_c} W_i^{Au} R_i^{Au}}. \quad (2)$$

Here, the  $W_i$  and  $R_i$  are the corresponding weighting factors and response functions for a certain time of flight channel, respectively. However, this approximation is only valid within 4 to 5%, because the pulse height spectra of captures on <sup>206</sup>Pb and <sup>197</sup>Au differ significantly near threshold (Fig. 1).

This effect has been taken into account in the determination of the experimental capture yield by simulating the capture cascades of each isotope as described in detail in Refs. [11, 18, 19]. Fig. 1 shows that the experimental spectra above the digital threshold are well reproduced by the simulations. With this correction the experimental yield becomes

$$Y^{exp} \propto \frac{f_{Pb}^t \sum_{320 keV}^{E_c} W_i^{Pb} R_i^{Pb}}{f_{Au}^t \sum_{320 keV}^{E_c} W_i^{Au} R_i^{Au}}. \quad (3)$$

For the adopted digital threshold the yield of the 4.9 eV resonance in <sup>197</sup>Au needs to be scaled by a factor  $f_{Au}^t = 1.071(3)$ , whereas the yield of the resonances in <sup>206</sup>Pb required a correction of  $f_{Pb}^t = 1.021(5)$  due to their harder spectrum. Hence, the correction factor of the final experimental yield was  $f^t = f_{Pb}^t / f_{Au}^t = 0.952(4)$ .

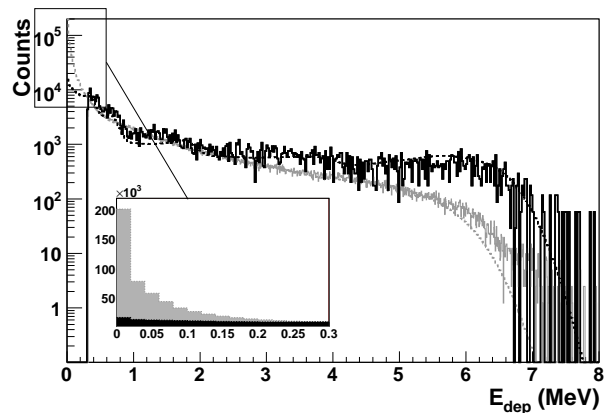


FIG. 1: Pulse height spectra for the 4.9 eV resonance in gold (grey) and for the 3.3 keV resonance in <sup>206</sup>Pb (black), arbitrarily scaled. The dashed lines are the MC-calculated  $\gamma$ -ray spectra for the two resonances. The linear scale used in the inset illustrates the large difference between the simulated spectra below a threshold of 300 keV.

## C. Angular distribution effects

Neutron capture with orbital angular momentum  $l > 0$  leads to an aligned state in the compound nucleus, perpendicular to the direction of the incident neutron. Given the small multiplicity ( $m = 1$  to 2) of the capture cascades in <sup>206</sup>Pb, most of the prompt  $\gamma$ -rays registered with the C<sub>6</sub>D<sub>6</sub> detectors still carry this anisotropy, which affects the measured yield. The angular distribution is in general given by,

$$W(\theta) = \sum_k A_k P_k(\cos\theta) = 1 + A_2 P_2(\cos\theta) + A_4 P_4(\cos\theta) + A_6 P_6(\cos\theta), \quad (4)$$

where  $P_k(\cos\theta)$  are the Legendre polynomials of order  $k$  and  $A_k$  are coefficients, which depend on the initial ( $J$ ) and final ( $J'$ ) spin values, on the multipolarity ( $l$ ) of the transition, and on the degree of alignment. The angular distribution effects in the capture yield are minimized (although not avoided) by setting the detectors at 125°. Since each C<sub>6</sub>D<sub>6</sub> detector covers a substantial solid angle, capture  $\gamma$ -rays are registered around  $125^\circ \pm \Delta\theta$ . For the actual setup of the present measurement one finds  $\Delta\theta \approx 28^\circ$ .

### 1. Resonances with spin $J = 1/2$

For resonances with  $J = 1/2$  it can be assumed that they decay directly to the ground state ( $J^\pi = 1/2^-$ ) or to the first or second excited states with  $J^\pi = 5/2^-$  and  $J^\pi = 3/2^-$ , respectively (see also Fig. 2). In these cases, one finds that  $A_2 = A_4 = A_6 = 0$ . Therefore, only resonances with spin  $J > 1/2$  may be affected by angular distribution effects.

TABLE I: Measured decay patterns from resonances with spin  $J = 3/2$  [14]. The systematic uncertainty in the yield of each resonance due to the angular distribution of the involved transitions are given in the last column.

$E_o$ (keV)	Intensity $I_\gamma$ (%)				$\sigma_\theta^{3/2^-}$
	$E_\gamma$ (keV)				
	6737.9	6168.6	5840.8	4114.5	
3.36	76.0(27)	2.5(8)	8.58(11)	13.0(8)	$\pm 10\%$
3.36 <sup>a</sup>	60	2.5	24.5	13	$\pm 8\%$
10.86		100			$\pm 2\%$
21.87		100			$\pm 2\%$
42.07			100		$\pm 10\%$

<sup>a</sup> This work.

## 2. Resonances with spin $J = 3/2$

In order to quantify the uncertainty due to the angular distribution of the prompt  $\gamma$ -rays emitted from excited states with  $J^\pi = 3/2^-$  the de-excitation patterns reported in Ref. [14] have been used (Table I).

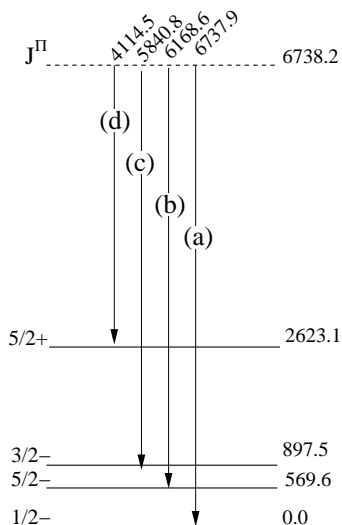


FIG. 2: Level scheme and decay patterns for  $^{207}\text{Pb}$  [14]. All energies are in keV.

For the first resonance at 3.36 keV, fair agreement has been found between the relative intensities of Ref. [14] and the rather coarse values deduced from the experimental pulse height spectrum (Table I and Fig. 1), which suffer from uncertainties due to background subtraction, limited counting statistics and poor energy resolution of the  $\text{C}_6\text{D}_6$  detectors. Therefore, an uncertainty of about 20% has to be ascribed to the quoted  $\gamma$ -ray intensities.

The estimated effect of the angular distribution on the capture yield ( $\sigma_\theta^{3/2^-}$ ) is given in the last column of Table I. These values were obtained via Monte Carlo simulations of the experimental setup, using the energies and intensities listed in Table I and the prescription of Ref. [20]. The main uncertainty in the calculation

of the angular distribution effects arises from the unknown admixtures of different multiplicities (M1+E2) for the transitions connecting the original excited state  $J^\pi = 3/2^-$  with any of the three lowest states (paths (a), (b) and (c) in Fig. 2). As shown in Table I, the decay pattern and the corresponding effect on the capture yield  $\sigma_\theta^{3/2^-}$  vary abruptly from one resonance to another. It is therefore difficult to assess a common systematic uncertainty for the remaining  $3/2^-$  resonances. Assuming that the four resonances listed in Table I constitute a representative sample, one may consider their standard deviation of  $\sigma = 4\%$  as a realistic estimate of the systematic uncertainty due to angular distribution effects.

Resonances with  $J^\pi = 3/2^+$  can be assumed to decay directly to the ground state through an E1 transition. In this case we have estimated an effect of 10% in the capture yield with respect to the isotropic case. However, since  $3/2^+$  resonances appear at a relatively high neutron energy, the final effect in the MACS is practically negligible (see below Sec. IV B).

## 3. Resonances with spin $J = 5/2$

For resonances in  $^{207}\text{Pb}$  with  $J^\pi = 5/2^+$  the most probable decay would be through an electric dipole transition to the first excited state with  $J^\pi = 5/2^-$  and/or to the second excited state with  $J^\pi = 3/2^-$  (paths (b) and (c) in Fig. 2). Under these assumptions, the effect on the capture yield would be -12% for path (b) and 9% for path (c). However, mixtures of both decay paths would partly compensate the correction for angular distribution effects. Adopting one standard deviation of the two extreme cases  $\sigma_\theta^{5/2^+} \simeq 10\%$  would, therefore, represent a rather conservative estimate of the corresponding uncertainty. Nevertheless, even such a relatively large uncertainty for the cross section of  $J^\pi = 5/2^+$  resonances would have negligible consequences for the Maxwellian averaged cross section because these resonances contribute very little to the total capture cross section (see Sec. IV B).

## D. Summary of uncertainties

With the WFs calculated via the Monte Carlo technique, the accuracy of the PHWT has been investigated in detail by the n\_TOF collaboration [18]. It has been shown that the capture yield can be determined from the measured raw data with an accuracy better than 2%.

Other sources of systematic uncertainty pertaining to this measurement are due to the energy dependence of the neutron flux ( $\pm 2\%$ ) and to the background due to in-beam  $\gamma$ -rays ( $\pm 1\%$ ). In the particular case of the  $(n, \gamma)$  cross section of  $^{206}\text{Pb}$ , the uncertainty introduced by the angular distribution of the capture  $\gamma$ -rays has to be considered as well. This effect has been estimated to

contribute an uncertainty of  $\pm 4\%$  for resonances with  $J^\pi = 3/2^-$  and less than  $\pm 10\%$  for resonances with  $J^\pi = 3/2^+, 5/2^+$ .

#### IV. RESULTS

A total of 61 capture levels were analyzed in the neutron energy range from 3 keV up to 570 keV using the R-matrix code SAMMY [21]. In the analysis, the orbital angular momenta  $l$  and the resonance spins  $J$  were adopted from Ref. [22]. Some of the  $l$  and  $J$  parameters listed in Table II are tentative or arbitrary if missing in Ref. [22]. We list all the parameters used in our analysis so that the final values can be recalculated if necessary. The capture yield  $Y(E_o, \Gamma_n, \Gamma_\gamma)$  was parameterized with the Reich-Moore formalism, and a channel radius of 9.5 fm was used for all partial waves. This parameterized

yield was fitted to the corrected experimental yield by variation of the capture width  $\Gamma_\gamma$  and/or neutron width  $\Gamma_n$ ,

$$f^t \times Y^{exp} = B + Y(E_o, \Gamma_n, \Gamma_\gamma), \quad (5)$$

where  $f^t$  is the global yield correction factor given in Sec. III B. The term  $B$  describing the background was parameterized as an analytical function of the neutron energy in the range between 1 eV and 30 keV. Beyond 30 keV,  $B$  was best described by means of a numerical function (pointwise) determined from the measurement of the  $^{208}\text{Pb}$  sample (see Ref. [23] for details). The uncertainties quoted for the energy of each resonance are only the statistical errors obtained from the fits of the capture data performed with SAMMY.

TABLE II: Resonance parameters derived from the R-matrix analysis of the  $^{206}\text{Pb}(n, \gamma)$  data.

$E_o$ (eV)	$l$	$J$	$\Gamma_\gamma$ (meV)	$\Delta\Gamma_\gamma$ (%)	$\Gamma_n$ (meV)	$\Delta\Gamma_n$ (%)	$K_r^a$ (meV)	$\Delta K_r$ (%)
3357.93(0.04)	1	3/2	78.1	3	235		117	2
10865.0(0.4)	1	3/2	64.9	9	44.1	8	52.5	6
11296.0(0.5)	(1)	(1/2)	455		44.6	7	40.6	7
14220.0(0.6)	1	(1/2)	152	6	1560		139	5
16428.0(0.4)	0	1/2	2268	9	936	5	662	5
19744.0(1.3)	1	(1/2)	156	7	2581		147	6
19809.0(0.9)	1	(3/2)	295		71.6	8	115	6
21885.0(0.9)	1	3/2	121	6	875		212	5
25112.0(0.9)	1	3/2	438	9	326	8	374	6
25428(5)	1	1/2	254	7	48901		253	7
36200(6)	1	1/2	312	14	35700		309	13
37480.0(1.9)	1	(3/2)	151	15	890		258	13
39028(2)	1	(1/2)	346		93.0	36	73.3	28
40647(2)	1	(1/2)	163	23	884		138	19
42083.0(1.7)	1	(3/2)	419	21	1419	91	647	26
47534(2)	(1)	(1/2)	184	34	1000		155	29
59233.0(0.2)	(2)	(3/2)	322	16	1000		487	12
63976(3)	(2)	5/2	151	17	1110		400	15
65990(10)	0	1/2	1186	9	82200		1169	9
66590(6)	1	3/2	198	19	9530		387	19
70352(7)	1	1/2	163	34	10780		161	34
80388(4)	2	3/2	1490	8	7005		2457	6
83699(6)	(2)	(3/2)	351	16	8000		673	15
88509(6)	2	5/2	375	13	7996		1076	12
91740(4)	(1)	(3/2)	298	25	1000		460	19
92620(13)	0	1/2	991	15	32000		961	15
93561(6)	2	3/2	125	37	7001		246	37
94743(7)	2	(3/2)	241	20	7000		465	20
101220(7)	2	(5/2)	119	26	8000		351	25
114380(5)	1	(3/2)	655	24	2500		1037	19
114602(6)	2	(5/2)	366	19	5600		1030	18
118100(6)	2	(5/2)	390	16	5100		1087	15
124753(47)	1	3/2	2972	9	300000		5886	9
125312(7)	2	(3/2)	2783	10	21005		4915	9
126138(38)	(1)	(3/2)	319	32	100000		635	32
140570(23)	2	3/2	1387	11	103000		2736	11
145201(6)	(2)	(3/2)	518	30	3100		888	26
146419(24)	0	1/2	6092	8	176000		5888	8

150880(7)	(1)	(1/2)	554	48	4400	492	43
151290(13)	2	5/2	457	23	19000	1340	22
191217(48)	(1)	(1/2)	767	28	96977	761	27
196990(37)	1	1/2	584	45	64000	579	44
198618(34)	2	3/2	2730	10	132108	5350	10
274630(22)	1	(1/2)	514	65	32000	506	64
276984(49)	2	3/2	2481	13	112000	4854	13
313400(18)	2	(3/2)	1020	32	22000	1950	31
314340(84)	2	5/2	964	24	179000	2875	24
356098(22)	2	(5/2)	676	35	31000	1985	35
357465(87)	2	3/2	1998	24	455000	3979	24
406200(55)	2	5/2	656	51	102000	1955	51
407200(41)	2	3/2	2906	24	71000	5583	23
416370(127)	2	5/2	2722	16	307000	8096	16
433340(32)	2	(5/2)	4122	17	47000	11368	16
434604(37)	(2)	(3/2)	4695	23	58000	8687	21
443412(13)	(2)	(5/2)	2375	21	14000	6092	18
466320(49)	(1)	(3/2)	5413	15	90000	10211	14
469080(76)	2	3/2	3222	19	161000	6317	19
471789(28)	(3)	(5/2)	792	36	41000	2330	35
476310(172)	0	1/2	5252	18	374000	5180	17
510690(51)	(2)	(3/2)	3123	18	86000	6026	18
572245(181)	2	5/2	3838	13	793194	11460	13

<sup>a</sup> Capture kernel  $K_r = g\Gamma_\gamma\Gamma_n/\Gamma$ , with  $g = J + 1/2$ .

### A. Comparison to previous work

The radiative neutron capture cross section of  $^{206}\text{Pb}$  has been measured at ORNL [14, 15, 24], at RPI [25] and at IRMM [26]. As representative examples of these measurements we consider in this section two measurements made at ORELA [14, 15], a more complete analysis [27] of the ORELA capture data [15] made in combination with transmission data [28] and the recent experiment made at IRMM [26]. In order to compare these four data sets with the present results (Table II), the ratio of the capture kernels are shown in Fig. 3.

The values reported in Ref. [15] show a relatively good agreement with our results, except for the first two resonances at 3.3 keV and 14.25 keV, which are lower by  $\sim 50\%$  (see Fig. 3). However, these two resonances and the resonance at 16.428 keV are important because of their dominant contribution to the MACS in the energy range between 5 keV and 20 keV. It is difficult to determine the source of discrepancy, thus no correlation has been found between the discrepancies and the spins of the resonances. The latter could probably help to determine if there is any effect related to the angular distribution of the prompt capture  $\gamma$ -rays or to the WF used in the previous measurement.

In the second measurement at ORELA [14] the discrepancies versus our present results are smaller (see Fig. 3), but the capture kernels are systematically larger, on average  $20\pm 5\%$  higher. This could probably reflect that the WF used in Ref. [14] is overweighting the relatively hard pulse height spectrum of  $^{207}\text{Pb}$ . Indeed, similar discrepancies have been found in the past for  $^{56}\text{Fe}$  [29], where the

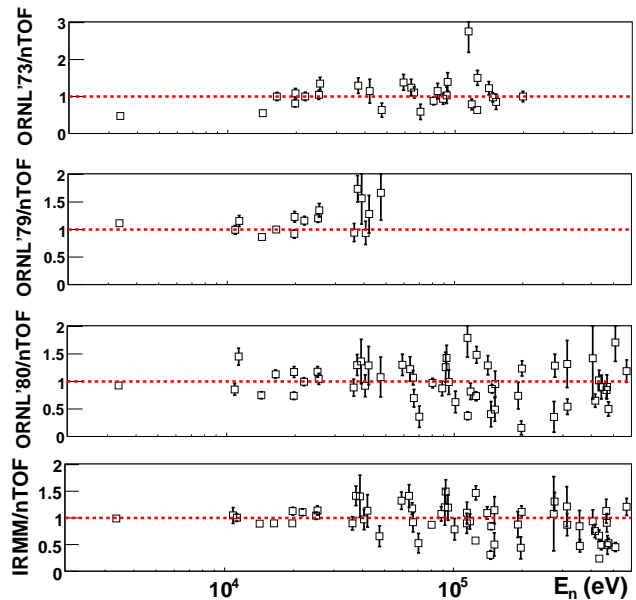


FIG. 3: (Color online) Ratio between the capture kernels reported in Ref. [15] (top), Ref. [14] (2nd), Ref. [27] (3rd) and Ref. [26] (bottom) and the kernels determined here.

pulse height spectrum is also considerably harder than that of the  $^{197}\text{Au}$  sample used for yield normalization.

The posterior analysis [27] of the ORELA capture data [15] in combination with transmission [28] shows, on average, better agreement with the capture areas reported here (see Fig. 3).

Finally, the results reported in the measurement at IRMM [26] show the best agreement with the capture kernels of n-TOF (see Fig. 3). At  $E_n \leq 40$  keV both measurements agree within a few percent. At higher en-

ergy the fluctuations are larger, but the agreement is still good within the quoted error bars.

As an illustrative example, the capture yield measured at n\_TOF for the first resonance at 3.3 keV is compared in the top panel of Fig. 4 versus the yield calculated from the resonance parameters reported in Refs. [14, 22, 26]. Obviously, the IRMM and n\_TOF results show good agreement in both the capture area and the resonance energy.

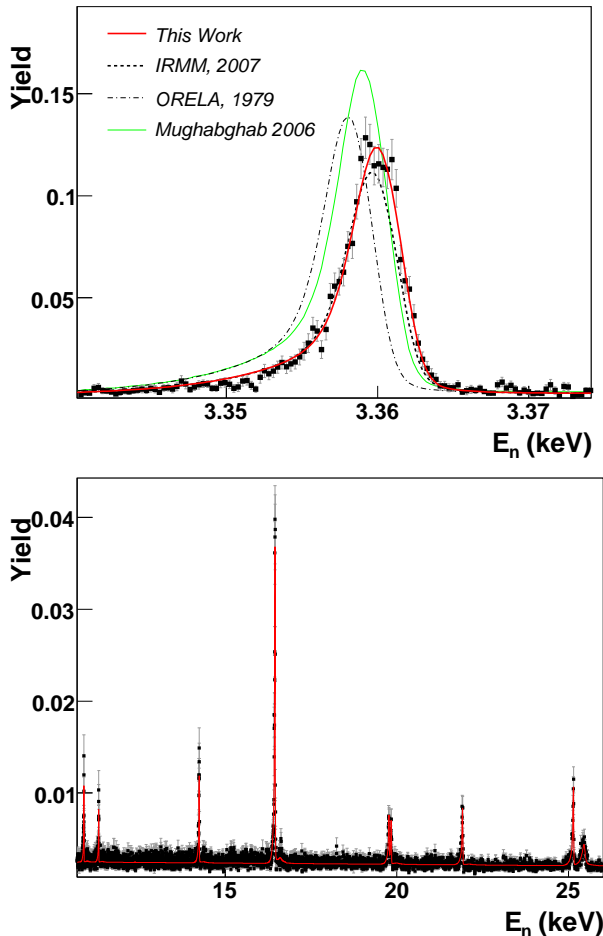


FIG. 4: (Color online) (Top figure) The bold red line represents an R-matrix fit to our experimental capture yield starting from the initial parameters (solid green line) in Ref. [22]. The dashed and dott-dashed curves correspond to the capture yields determined in Ref. [26] and Ref. [14], respectively. (Bottom figure) The fitted capture yield in the 10-30 keV energy range (thin red line).

### B. Maxwellian averaged capture cross section

The Maxwellian averaged cross section (MACS) was determined using the SAMMY code in the range of thermal energies relevant for stellar nucleosynthesis, i.e. from  $kT=5$  keV up to  $kT=50$  keV. As discussed in the previous section, our results agree best with the values re-

ported in Ref. [26]. The latter data set seems also to be the most complete in terms of number of analyzed resonances, with about 283 levels. Therefore our results were complemented with resonances from Ref. [26] in order to avoid any discrepancy due to resonances missing in Table II. The contribution of these supplementary resonances to the MACS is  $< 0.1\%$  at  $kT = 5$  keV and  $6\%$  at  $kT = 25$  keV. The fact that this correction starts to be significant towards  $kT \gtrsim 25$  keV is not relevant for the study of the nucleosynthesis of  $^{206}\text{Pb}$ . Indeed, as it is discussed below in Sec. V,  $^{206}\text{Pb}$  is mostly synthesized between the He-shell flashes of the asymptotic giant branch stars. These intervals between pulses provide about 95% of the neutron exposure via the  $^{13}\text{C}(\alpha, n)^{16}\text{O}$  reaction, which operates at a thermal energy of  $kT = 8$  keV. At this stellar temperature less than 0.5% of the MACS is due to the supplemented resonances.

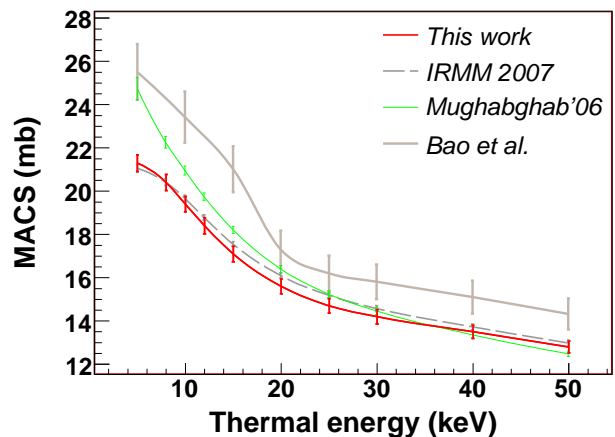


FIG. 5: (Color online) Maxwellian averaged  $(n, \gamma)$  cross sections for  $^{206}\text{Pb}$  from the resonance parameters of this work (bold red) compared to the IRMM measurement [26] (dashed), to the recommended data of Ref. [30] (grey) and to the compiled data of Ref. [22] (solid green).

The uncertainties shown in Fig. 5 are only statistical. The systematic uncertainties of the MACS quoted in Table III include all contributions discussed in Sec. III D.

TABLE III: Maxwellian averaged cross section for  $^{206}\text{Pb}$ .

Thermal energy $kT$ (keV)	MACS (mbarn)	$\sigma_{stat}$ (%)	$\sigma_{sys}$ (%)
5	21.3	1.8	5
8	20.4	1.8	3
10	19.4	1.9	3
12	18.4	2.0	3
15	17.1	2.1	3
20	15.6	2.2	3
25	14.7	2.3	3
30	14.2	2.3	4
40	13.5	2.2	4
50	12.8	2.1	4

Assuming systematic uncertainties of 4% and 10% for



$3/2^-$  and  $5/2^-$  resonances, respectively, the final uncertainties are completely dominated by the 4% uncertainty of the  $3/2^-$  resonances. A change of 10% in the cross section of the fewer  $5/2^+$  resonances has a negligible influence on the MACS at  $kT = 5$  keV, it contributes only 0.5% at  $kT = 25$  keV and increases linearly up to 1% at  $kT = 50$  keV. An effect of 10% in the capture yield of the  $3/2^+$  resonances makes only a 1% difference in the MACS at  $kT = 25$  keV and it becomes also negligible towards lower stellar temperatures. The 3% systematic uncertainty of the experimental method itself originates from the PHWT, the neutron flux shape, and the use of the saturated resonance technique.

In summary, the MACS of  $^{206}\text{Pb}$  can now be given with total uncertainties of 5% and 4% at the stellar temperatures corresponding to 5 keV and 25 keV thermal energies, respectively. This improvement with respect to the previously recommended values of Ref. [30] becomes particularly important for determining the  $s$ -process contribution to the production of lead and bismuth in the Galaxy.

## V. THE $s$ -PROCESS ABUNDANCE OF $^{206}\text{Pb}$ AS A CONSTRAINT FOR THE U/TH CLOCK

The  $s$ -process production of  $^{206}\text{Pb}$  takes place in low mass asymptotic giant branch (AGB) stars of low metallicity [31], where about 95% of the neutron exposure is provided by the  $^{13}\text{C}(\alpha, n)^{16}\text{O}$  reaction at a thermal energy of  $kT \approx 8$  keV. At this stellar temperature the present MACS is about 20% lower and two times more accurate (see Fig. 5) than the values from Ref. [30], which have been commonly used so far for stellar nucleosynthesis calculations. The additional neutron irradiation provided by the  $^{22}\text{Ne}(\alpha, n)^{25}\text{Mg}$  reaction at the higher thermal energy of  $kT = 23$  keV during the He shell flash is rather weak.

With the new MACS the  $s$ -process abundance of  $^{206}\text{Pb}$  has been re-determined more accurately. A model calculation was carried out for thermally pulsing AGB stars of 1.5 and 3  $M_{\odot}$  and a metallicity of  $[\text{Fe}/\text{H}] = -0.3$ . The abundance of  $^{206}\text{Pb}$  is well described by the average of the two stellar models, which represent the so-called main component [32]. Since the contribution of  $^{206}\text{Pb}$  by the strong component is only 2%, the main component can be used to approximate the effective production of  $^{206}\text{Pb}$  during Galactic chemical evolution (GCE) [31, 33, 34]. This approach yields an  $s$ -process abundance of  $^{206}\text{Pb}$ , which represents 70(6)% of the solar abundance value  $N_{\odot}^{206} = 0.601(47)/10^6\text{Si}$  [35]. The same calculation made with the older MACS recommended by Bao et al. [30] yields 64%. The uncertainty on the calculated  $s$ -process abundance is mostly due to the uncertainty on the solar abundance of lead (7.8%) [36]. The contribution from the uncertainty on the MACS at 8 keV is less than 2%. Finally, the contribution from the  $s$ -process model is  $\pm 3\%$ . The latter corresponds to the mean root square devi-

ation between observed and calculated abundances for  $s$ -process only isotopes [32]. This uncertainty is justified for  $^{206}\text{Pb}$  because its nucleosynthesis is dominated by the main component and it is only marginally affected ( $\sim 2\%$ ) by the strong component [31, 32, 33, 34]. Furthermore, because of the much lower cross sections of  $^{208}\text{Pb}$  and  $^{209}\text{Bi}$ , the synthesis of  $^{206}\text{Pb}$  remains practically unaffected by the  $\alpha$ -recycling after  $^{209}\text{Bi}$  [7]. This lends further confidence that the production of  $^{206}\text{Pb}$ , and hence its uncertainty, follows the same trend as the main  $s$ -process component.

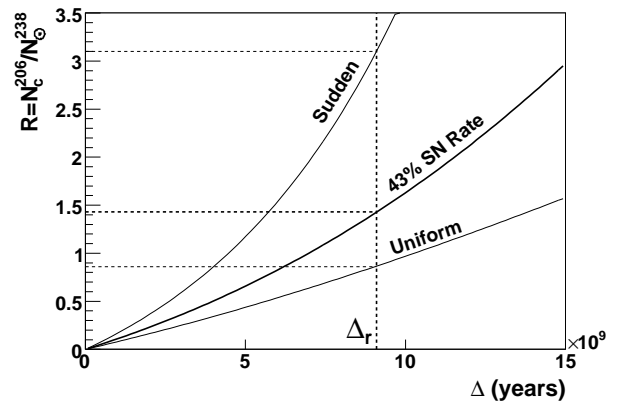


FIG. 6: Estimate of the radiogenic component of  $^{206}\text{Pb}$  using the Fowler's model with different nucleosynthetic assumptions (see labels in curves) and the  $r$ -process age  $\Delta_r = t_U - 4.6$  Gyr (vertical dashed line) derived from the age of the Universe  $t_U$  [37].

In order to estimate a constraint for the  $r$ -process abundance of  $^{206}\text{Pb}$  one needs to take into account its radiogenic contribution,  $N_c^{206}$ , due to the decay of  $^{238}\text{U}$ . As it is shown in the following, this component is relatively small but can not be neglected. Based on the schematic model of Fowler, which assumes an exponential decrease of the  $r$ -process yield during GCE [4] (supernova rate  $\Lambda = (0.43t)^{-1} \text{Gyr}^{-1}$ ) and using the current best estimates for the age of the Universe ( $t_U = 13.7 \pm 0.2$  Gyr) [37], one obtains  $N_c^{206} = 0.027(2)/10^6\text{Si}$  (see Fig. 6 and Table IV). This number, combined with our result for  $N_s^{206}$ , yields an  $r$ -process residual,

$$N_r^{206} = N_{\odot}^{206} - N_s^{206} - N_c^{206} = 0.153 \pm 0.063. \quad (6)$$

The uncertainty in this result includes contributions of 8.4% from  $N_c^{206}$  (corresponding to the uncertainty on the solar abundance of  $^{238}\text{U}$  [36]), 7.8% from the total solar abundance of  $^{206}\text{Pb}$ ,  $N_{\odot}^{206}$  [35, 36], and 8.6% from the determination of  $N_s^{206}$  as discussed above. This means that, apart from the uncertainties related with the simplified assumptions in the GCE model of Fowler, the  $r$ -process abundance can be reliably constrained between 16% and 36% of the solar  $^{206}\text{Pb}$ .

The  $r$ -process residuals derived here are consistent with  $r$ -process model calculations available in the liter-

TABLE IV: Radiogenic abundance of  $^{206}\text{Pb}$ ,  $N_c^{206}$  (Si=10<sup>6</sup>), derived from the model of Fowler and the age of the Universe (see Fig. 6).  $r$ -Process residuals obtained via eq. 6.

GCE (Fig. 6)	$N_c^{206} = RN_{\odot}^{238}$ 10 <sup>6</sup> Si	$N_r^{206} = N_{\odot}^{206} - N_s^{206} - N_c^{206}$ 10 <sup>6</sup> Si	$N_r^{206}/N_{\odot}^{206}$ (%)
43% SN rate	0.027(2)	0.15(6)	26(10)
Sudden	0.058(5)	0.12(6)	20(10)
Uniform	0.0161(14)	0.16(6)	27(10)

TABLE V: Radiogenic abundance of  $^{207}\text{Pb}$ ,  $N_c^{207}$  (Si=10<sup>6</sup>), derived from the model of Fowler and the age of the Universe.  $r$ -Process residuals obtained via eq. 6.

GCE	$N_c^{207} = RN_{\odot}^{235}$ 10 <sup>6</sup> Si	$N_r^{207} = N_{\odot}^{207} - N_s^{207} - N_c^{207}$ 10 <sup>6</sup> Si	$N_r^{207}/N_{\odot}^{207}$ (%)
43% SN rate	0.150(13)	0.003(73)	0(11)
90% SN rate	0.08(7)	0.073(72)	11(11)
Uniform	0.047(4)	0.106(72)	16(11)

ature, i.e.,  $N_r^{206} = 26.6\%$  [1]. More recent calculations yield  $N_r^{206}$  values between 27% and 35% [3]. One can also derive hard limits for the  $r$ -process abundance, considering the two extreme cases of sudden nucleosynthesis ( $\Lambda \rightarrow \infty$ ) and uniform nucleosynthesis ( $\Lambda \rightarrow 0$ ). This yields constraints between 10% and 37% of solar  $^{206}\text{Pb}$  (see Table IV).

The situation is rather different for the corresponding  $^{207}\text{Pb}/^{235}\text{U}$  ratio, which has been investigated as a potential clock in the past [38]. In this case, the  $s$ -process abundance of  $^{207}\text{Pb}$  was recently determined to be  $N_s^{207} = 77(8)\%$  [19]. A similar calculation to that shown in Fig. 6 gives  $N_c^{207} = 0.150(13)$  (see Table V). The latter value reflects the large relative radiogenic abundance of  $^{207}\text{Pb}$ ,  $N_c^{207}/N_{\odot}^{207} = 22\%$ , due to the much shorter half-life of  $^{235}\text{U}$ . From the total solar abundance of  $^{207}\text{Pb}$  [35] and the  $N_s^{207}$  and  $N_c^{207}$  values quoted above, the  $r$ -process residual becomes  $N_r^{207} = 0.003 \pm 0.073$ , which means that  $N_r^{207}$  can not be larger than 11% of the  $^{207}\text{Pb}$  abundance in the solar system,  $N_{\odot}^{207} = 0.665(52)$  [35] (Table V).

This result is in contrast with  $r$ -process model calculations, which yield values between 22.7% and 25.3%, with a relative uncertainty of 15-20% [1, 3]. The  $s$ -process abundances of  $^{206,207}\text{Pb}$  are rather reliable and not very sensitive to details of the stellar models [7, 39]. Therefore, this discrepancy indicates that  $r$ -process abundances might have been overestimated, possibly because the odd-even effect is not properly reproduced by the ETFSI-Q mass model implemented in the  $r$ -process cal-

culations [1, 3]. Indeed, one needs to increase the supernova rate in the standard Fowler model from 43% up to 90% ( $\Lambda = (0.90t)^{-1} \text{ Gyr}^{-1}$ ) in order to achieve agreement between these  $r$ -process constraints and the latter  $r$ -process calculations [1, 3]. Obviously the less realistic uniform scenario would also provide agreement with the abundances from these  $r$ -process models (see Table V).

However the situation has been improved recently after more detailed  $r$ -process model calculations [40] predicted a new  $N_r^{207}$  value, which is 35% lower than the previous one of Ref. [1]. This yields  $N_r^{207}/N_{\odot}^{207} = 16.8\%$ , which is substantially closer (considering an uncertainty of 20%) to the upper limit of 11% derived here. In this case a good agreement would be found for a more reasonable increase of the supernova rate to 55% in the Fowler model.

These constraints for the  $r$ -process abundances of  $^{206,207}\text{Pb}$  become relevant for the validation of  $r$ -process model calculations and hence, for the reliable interpretation of actinide abundances observed in UMP stars and their use as cosmochronometers.

The  $s$ -process aspects will be more rigorously investigated in a comprehensive study of the Pb/Bi region [41], where the role of stellar modeling and GCE will be discussed with a complete set of new cross sections for the involved isotopes, including the present data for  $^{206}\text{Pb}$ , and recent results for  $^{204}\text{Pb}$  [23],  $^{207}\text{Pb}$  [19] and  $^{209}\text{Bi}$  [11].

## VI. SUMMARY

The neutron capture cross section of  $^{206}\text{Pb}$  as a function of the neutron energy has been measured with high resolution at the CERN n\_TOF installation using two C<sub>6</sub>D<sub>6</sub> detectors. Capture widths and/or radiative kernels could be determined for 131 resonances in the neutron energy interval from 3 keV up to 620 keV. Systematic uncertainties of 3%, 5%, and  $\lesssim 10\%$  were obtained for resonances with spin-parities of  $1/2^{\pm}$ ,  $3/2^{-}$  and  $5/2^{+}$ , respectively. The Maxwellian averaged cross sections were found to be significantly smaller by 10% to 20% compared to values reported earlier [30], resulting in a correspondingly enhanced  $s$ -process production of  $^{206}\text{Pb}$ . First calculations with a standard AGB model yield an  $s$ -process component of 70(6)% for the  $^{206}\text{Pb}$  abundance. Combined with an estimate of the radiogenic production of  $^{206}\text{Pb}$ , the  $r$ -process abundance is constrained between 16% and 36% of the solar  $^{206}\text{Pb}$  abundance, well in agreement with  $r$ -process model calculations reported in the literature [1, 3]. A similar analysis for  $^{207}\text{Pb}$  shows agreement only with most recent  $r$ -process model calculations [40].

[1] J. J. Cowan, B. Pfeiffer, K.-L. Kratz, F.-K. Thielemann, C. Sneden, S. Burles, D. Tytler, and T. C. Beers, *Astrophys. J.* **521**, 194 (1999).

[2] H. Schatz, R. Toenjes, B. Pfeiffer, T. C. Beers, J. J. Cowan, V. Hill, and K.-L. Kratz, *Astrophys. J.* **579**, 626 (2002).

- [3] K.-L. Kratz, B. Pfeiffer, J. J. Cowan, and C. Sneden, *New Astronomy Review* **48**, 105 (2004).
- [4] D. D. Clayton, *Astrophys. J.* **139**, 637 (1964).
- [5] W. A. Fowler and F. Hoyle, *Astrophys. J.* **65**, 345 (1960).
- [6] A. Herrera *et al.*, in *Workshop on Nuclear Data for the Transmutation of Nuclear Waste*, edited by A. Kelic and K. Schmidt (2003), GSI-Darmstadt, Germany. ISBN 3-00-012276-1.
- [7] U. Ratzel, C. Arlandini, F. Käppeler, A. Couture, M. Wiescher, R. Reifarth, R. Gallino, A. Mengoni, and C. Travaglio, *Phys. Rev. C* **70**, 065803 (2004).
- [8] U. Abbondanno *et al.* (2002), CERN n\_TOF Facility: Performance Report, CERN/INTC-O-011 INTC-2002-037 CERN-SL-2002-053ECT.
- [9] U. Abbondanno *et al.*, *Nuclear Instruments and Methods in Physics Research A* **538**, 692 (2005).
- [10] R. Plag, M. Heil, F. Käppeler, P. Pavlopoulos, R. Reifarth, and K. Wisshak, *Nuclear Instruments and Methods in Physics Research A* **496**, 425 (2003).
- [11] C. Domingo-Pardo *et al.*, *Phys. Rev. C* **74**, 025807 (2006).
- [12] R. Macklin, J. Halperin, and R. Winters, *Nuclear Instruments and Methods in Physics Research A* **164**, 213 (1979).
- [13] C. Borcea *et al.*, *Nuclear Instruments and Methods in Physics Research A* **513**, 524 (2003).
- [14] M. Mizumoto, S. Raman, R. L. Macklin, G. G. Slaughter, J. A. Harvey, and J. H. Hamilton, *Phys. Rev. C* **19**, 335 (1979).
- [15] B. Allen, R. Macklin, R. Winters, and C. Fu, *Phys. Rev. C* **8**, 1504 (1973).
- [16] U. Abbondanno *et al.* (2003), Tech. Rep. CERN-SL-2002-053 ECT.
- [17] R. L. Macklin and J. H. Gibbons, *Phys. Rev.* **159**, 1007 (1967).
- [18] U. Abbondanno *et al.*, *Nuclear Instruments and Methods in Physics Research A* **521**, 454 (2004).
- [19] C. Domingo-Pardo *et al.*, *Phys. Rev. C* **74**, 055802 (2006).
- [20] A.J. Ferguson, *Angular correlation methods in gamma-ray spectroscopy* (North-Holland Publishing Company-Amsterdam, 1965).
- [21] N. M. Larson (2006), "Updated users' guide for SAMMY: Multilevel R-matrix fits to neutron data using Bayes' equations", SAMMY, computer code Report ORNL/TM-9179/R7, Oak Ridge National Laboratory.
- [22] S.F. Mughabghab (2006), *Neutron Cross Sections: Neutron Resonance Parameters and Thermal Cross Sections*, Academic press.
- [23] C. Domingo-Pardo, U. Abbondanno, G. Aerts, H. Álvarez-Pol, F. Alvarez-Velarde, S. Andriamonje, J. Andrzejewski, P. Assimakopoulos, L. Audouin, G. Badurek, et al., *Phys. Rev. C* **75**, 015806 (2007), arXiv:nucl-ex/0610033.
- [24] R. L. Macklin, P. J. Pasma, and J. H. Gibbons, *Physical Review* **136**, 695 (1964).
- [25] Z.M. Bartolome *et al.*, Progress Report, Rensselaer Polytechnic Institute (1969), RPI-328-160,7,69.
- [26] A. Borella, F. Gunsing, M. Moxon, P. Schillebeeckx, and P. Siegler, *Phys. Rev. C* **76**, 014605 (2007).
- [27] B. J. Allen, A. R. D. Musgrove, J. W. Boldeman, M. J. Kenny, and R. L. Macklin, Progress Report 46 (1980), Australian AEC Progress report.
- [28] D. J. Horen, J. A. Harvey, and N. W. Hill, *Phys. Rev. C* **20**, 478 (1979).
- [29] R. Macklin, *Nucl. Sci. Eng.* **95**, 200 (1987).
- [30] Z. Y. Bao, H. Beer, F. Käppeler, F. Voss, K. Wisshak, and T. Rauscher, *Atomic Data and Nuclear Data Tables* **76**, 70 (2000).
- [31] C. Travaglio, R. Gallino, M. Busso, and R. Gratton, *Astrophys. J.* **549**, 346 (2001).
- [32] C. Arlandini, F. Käppeler, K. Wisshak, R. Gallino, M. Lugaro, M. Busso, and O. Straniero, *Astrophys. J.* **525**, 886 (1999).
- [33] C. Travaglio, D. Galli, R. Gallino, M. Busso, F. Ferrini, and O. Straniero, *Astrophys. J.* **521**, 691 (1999).
- [34] R. Gallino, C. Arlandini, M. Busso, M. Lugaro, C. Travaglio, O. Straniero, A. Chieffi, and M. Limongi, *Astrophys. J.* **497**, 388 (1998).
- [35] K. Lodders, *Astrophys. J.* **591**, 1220 (2003).
- [36] N. Grevesse and E. Anders, in *AIP Conf. Proc. 183: Cosmic Abundances of Matter*, edited by C. J. Waddington (1989), pp. 1-8.
- [37] C. L. Bennett, M. Halpern, G. Hinshaw, N. Jarosik, A. Kogut, M. Limon, S. S. Meyer, L. Page, D. N. Spergel, G. S. Tucker, et al., *Astrophys. J.* **148**, 1 (2003).
- [38] H. Beer and R. L. Macklin, *Phys. Rev. C* **32**, 738 (1985).
- [39] C. Domingo-Pardo, Ph.D. thesis, CSIC-University of Valencia (2005).
- [40] K.-L. Kratz (2007), "FRANZ Workshop on experimental opportunities for nuclear astrophysics at the Frankfurt neutron source of the Stern-Gerlach-Zentrum".
- [41] S. Bisterzo, R. Gallino, F. Käppeler, and C. Domingo-Pardo, *Astrophys. J.* (in preparation).